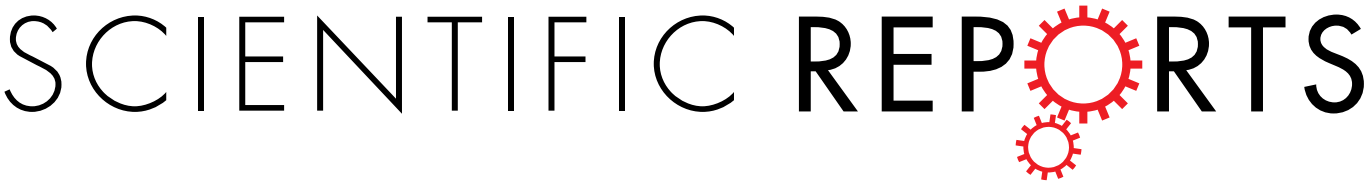

OPEN

# *In situ* observation of macroscopic phase separation in cobalt hexacyanoferrate film

Received: 22 July 2016
Accepted: 13 January 2017
Published: 16 February 2017

Masamitsu Takachi[1] & Yutaka Moritomo[1,2,3,4]

**Lithium-ion secondary batteries (LIBs) store electric energy via $Li^+$ deintercalation from cathode materials. The $Li^+$ deintercalation frequently drives a first-order phase transition of the cathode material as a result of the Li-ordering or Li-concentration effect and causes a phase separation (PS) into the Li-rich and Li-poor phases. Here, we performed an *in situ* microscopic investigation of the PS dynamics in thin films of cobalt hexacyanoferrate, $Li_xCo[Fe(CN)_6]_{0.9}$, against $Li^+$ deintercalation. The thick film ($d = 1.5\,\mu m$) shows a characteristic macroscopic PS of several tens of μm into the green ($Li_{1.6}Co[Fe(CN)_6]_{0.9}$) and black ($Li_{.6}Co[Fe(CN)_6]_{0.9}$) phases in the $x$ range of $1.0 < x < 1.6$. Reflecting the substrate strain, the thin film ($d = 0.5\,\mu m$) shows no trace of the PS in the entire $x$ region. Our observation suggests that the macroscopic PS plays a significant role in the charge/discharge dynamics of the cathode.**

The lithium-ion secondary battery (LIB)[1,2] is a widely used energy storage device for consumer electronics, such as smart phones and portable computers, and for electric vehicle power systems. In addition, the LIB is a key technology for multiple clean energy applications. Their energy and power densities are predominantly governed by the cathode materials, which store $Li^+$ within their crystal structure. Most commercialized cathode materials, such as $LiCoO_2$[3], $LiMn_2O_4$[4], and $Li(Ni_{1/3}Co_{1/3}Mn_{1/3})O_2$[5], form solid solutions over a large Li-concentration range. They do, however, show first-order structural phase transitions because of the Li-ordering or Li-concentration effect. These phase transitions cause phase separation (PS) into Li-rich and Li-poor phases, because the local Li concentration is the order parameter. For the purposes of this discussion, we classify the PS into two types, i.e., microscopic PS within the particle and macroscopic PS between the particles. The microscopic PS is initiated by nucleation of the second phase, whose size is determined by the balance between the free energy gain due to the phase transformation and the strain loss at the interface. In this case, the $Li^+$ deintercalation process suffers extra kinetic barriers, such as nucleation and the resultant interface strain within the particle. On the other hand, the macroscopic PS is advantageous for battery performance because particle homogeneity reduces the inner stresses and possible mechanical degradation of the material.

The PS problem is most extensively investigated in $LiFePO_4$[6], which stores Li through a two-phase transformation between $FePO_4$ and $LiFePO_4$[7–10]. $LiFePO_4$ shows very high rate performance resulting from smaller nanoparticles, doping, and surface coatings[11], although both the phases show low ionic and electronic conductivities. The transmission electron microscopy (TEM) images of chemically deintercalated $Li_{1/2}FePO_4$ nanoparticles show clear stripe-type phase boundaries within the particle[12]. This microscopic PS is well reproduced by a phase-field model including the elastic coherency strain[13]. On the other hand, Delmas and coworkers[14] investigated electrochemically deintercalated $Li_xFePO_4$ nanoparticles by means of X-ray diffraction and electron microscopy. They concluded that individual particles are essentially $FePO_4$ or $LiFePO_4$ (macroscopic PS). They interrupted the observation in terms of the 'domino-cascade model,' that is, $Li^+$ deintercalation takes place just near the phase boundary because nucleation of a new micro-domain of $FePO_4$ in another part of the $LiFePO_4$ crystal would require much higher energy. Based on the ab initio density functional calculations of $Li_xFePO_4$, Malik *et al.*[15] proposed that the transformation path to the single phase exists even at a very low overpotential. Thus, the PS problems in $LiFePO_4$ are still controversial.

[1]Graduate School of Pure and Applied Science, University of Tsukuba, Tsukuba 305-8571, Japan. [2]Center for Integrated Research in Fundamental Science and Engineering (CiRfSE), University Tsukuba, Tsukuba 305-8571, Japan. [3]Tsukuba Research Center for Interdisciplinary Materials Sciences (TIMS), University of Tsukuba, Tsukuba 305-8571, Japan. [4]Faculty of Pure and Applied Science, University of Tsukuba, Tsukuba 305-8571, Japan. Correspondence and requests for materials should be addressed to Y.M. (email: moritomo.yutaka.gf@u.tsukuba.ac.jp)

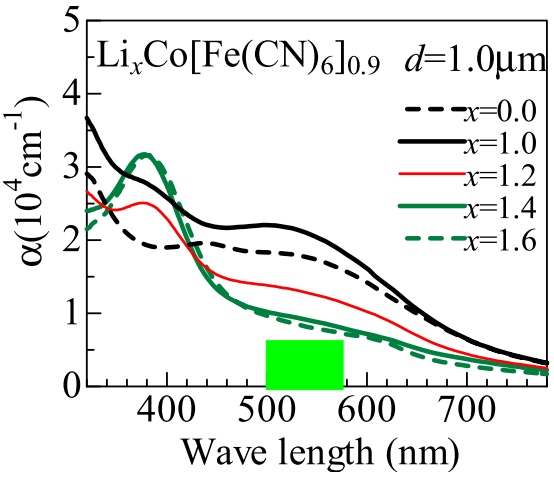


**Figure 1.** Absorption spectra of $Li_xCo[Fe(CN)_6]_{0.9}$ film ($d = 1.0\,\mu m$) against $x$. The green square represents the probe light source in the microscopy investigation.

Thin film of cobalt hexacyanoferrate, $Li_xCo[Fe(CN)_6]_{0.9}$, is another ideal platform to investigate the PS dynamics against $Li^+$ deintercalation. In addition, yhe $Li_xCo[Fe(CN)_6]_{0.9}$ film is a promising cathode material for LIB, showing a discharge capacity of 139 mAh/g and average voltage of 3.6 V[16]. Let us consider the structural correlation between $Li_xFePO_4$ and $Li_xCo[Fe(CN)_6]_{0.9}$. $Li_xFePO_4$ is built up of two-dimensional (2D) sheets with $[FeO_4]_n$ formula of corner-sheared $FeO_6$ octahedra. These sheets are connected by $PO_4$ tetrahedra to make a three-dimensional (3D) skeleton. The $Li^+$ deintercalation oxidizes $Fe^{2+}$ to $Fe^{3+}$ and causes significant change in the Fe-O bond length, which leads to the PS. On the other hands, $Li_xCo[Fe(CN)_6]_{0.9}$ is built up of $[Fe(CN)_6]^{4-}$ octahedra. Similarly to the case of $Li_xFePO_4$, these octahedra are connected by $Co^{2+}$ ions to make a 3D skeleton. The $Li^+$ deintercalation oxidizes $Co^{2+}$ to $Co^{3+}$ and causes significant change in the Co-N bond length, which leads the PS into the green (high-$x$) and black (low-$x$) phases at $x$~1.2[16]. The green and black phases show the face-centered cubic structure and are formally expressed as $Li_{1.6}Co^{2+}$ $[Fe^{2+}$ $(CN)_6]_{0.9}$ and $Li_{0.6}Co^{3+}$ $[Fe^{2+}$ $(CN)_6]_{0.9}$, respectively. Importantly, phase transformation into the black phase causes significant volume contraction: lattice constants ($a$) are 1.02 nm in the green phase and 1.00 nm in the black phase. The volume change is ascribed to the oxidization and resultant spin state transition of Co. Actually, the X-ray absorption near-edge structure (XANES) around the Co K-edge[16] indicates that $Co^{2+}$ and $Co^{3+}$ take the high-spin and low-spin states, respectively. Thus, in both the materials, the $Li^+$ deintercalation, and resultant oxidization of the 3D skeletons, causes the cooperative structural distortion and PS.

Here, we performed an *in situ* microscopic investigation of PS dynamics in the $Li_xCo[Fe(CN)_6]_{0.9}$ films with use of the color difference between the green and black phases against $Li^+$ deintercalation. In thick film ($d = 1.5\,\mu m$), we observed a characteristic macroscopic PS of several tens of μm into the original green and secondary black phases below $x < 1.0$. The length scale (several tens of μm) is much larger than the crystal grain size (several hundreds of nm). We, however, observed no trace of the PS in thin film ($d = 0.5\,\mu m$) and ascribed the absence of the PS to the strain due to the substrate.

## *In Situ* Observation of PS Dynamics

Figure 1 shows absorption spectra of the $Li_xCo[Fe(CN)_6]_{0.9}$ film against $x$. The film thickness ($d = 1.0\,\mu m$) was chosen so that the minimum transmittance (at 380 nm) becomes ~0.04. The spot of the light source is about 1 mm in diameter. Roughly speaking, the spectra at $x = 1.6$ and 1.0 corresponds to the green and black phases, respectively. In the green phase, the intense absorption observed around 380 nm is ascribed to the electron transfer from $Fe^{2+}$ to the neighboring $Co^{2+}$ [17]. In the black phase, the broad absorption observed around 540 nm is ascribed to the electron transfer from $Fe^{2+}$ to the neighboring $Co^{3+}$ [17]. The absorption intensity at 540 nm shows significant change in the phase transformation from the green to black phases. So, the 540 nm bands can be used as a sensitive monitor of the respective phases. The perpetration depth at the probe light wavelength is 0.4–1.0 μm. The minimum transmittance at the probe light wavelength is 0.04 even for the thickest ($d = 1.5\,\mu m$) film.

Figure 2 shows the charge curve of the $Li_xCo[Fe(CN)_6]_{0.9}$ film ($d = 1.5\,\mu m$) at 0.7 C against $x$, together with the microscopic images. In the late stage ($0.6 < x < 0.0$) of the charge curve, a plateau is observed at around 4.0 V. This plateau is ascribed to the reduction process of $Fe^{2+}$ to $Fe^{3+}$ [16]. At $x = 1.6$, the microscopic image is homogeneous and green, indicating that the system is in the green phase ($Li_{1.6}Co^{2+}$ $[Fe^{2+}$ $(CN)_6]_{0.9}$). With decreases in $x$, the black region appears ($x = 1.4$), increases in area ($x = 1.2$ and 1.0), and finally covers the entire image ($x = 0.8$). The black region corresponds to the black phase ($Li_{0.6}Co^{3+}$ $[Fe^{2+}$ $(CN)_6]_{0.9}$) because the region does not transmit the green light (Fig. 1). Thus, we observed macroscopic PS in thick film. We performed Rietveld structural analysis (Rietan-FP[18]) of the synchrotron-radiation X-ray powder diffraction pattern of $Li_{1.2}Co[Fe(CN)_6]_{0.9}$ (Fig. 3S). The $a$ values of the green and black phases are $1.01848 \pm 0.00006$ nm and $0.99535 \pm 0.00007$ nm, respectively. With further decrease in $x$ below $x = 0.8$, the image gradually becomes bright. This is because parts of $Fe^{2+}$, which is the final state of the optical transition, are oxidized to $Fe^{3+}$ with decrease in $x$.

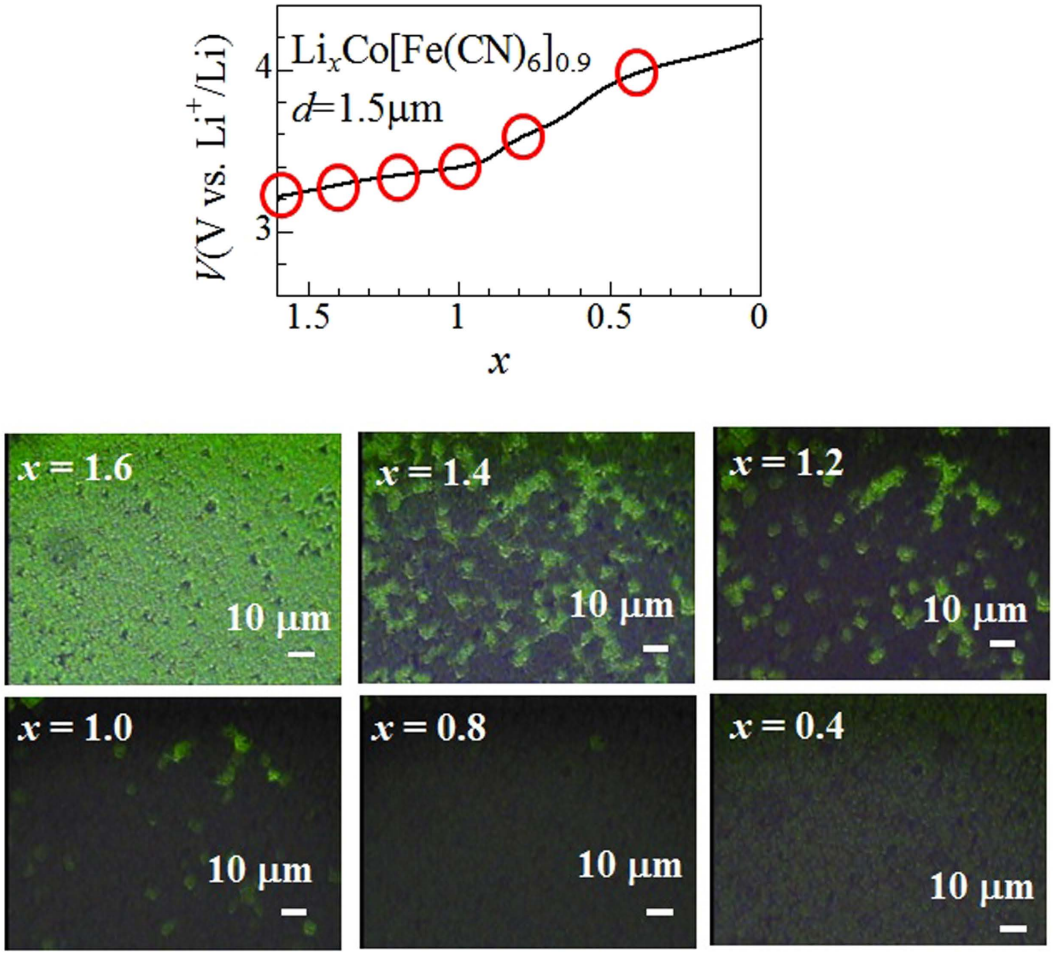


**Figure 2.** Upper panel: charge curve of $Li_xCo[Fe(CN)_6]_{0.9}$ film ($d = 1.5\,\mu m$) at 0.7 C against $x$. Lower panel: microscopic images at respective $x$, indicated by red circles in the 1st charge curve. Green and black regions at $x = 1.0$, 1.2, and 1.4 corresponds to the green and black phases, respectively.

Looking at Fig. 2 (the $x = 1.4$, 1.2, and 1.0 images), the size of the green region gradually shrinks without changing the contrast, indicating that no additional nucleation of the black micro-domain occurs within the green region. That is, the transformation from green ($Li_{1.6}Co^{2+}$ $[Fe^{2+}(CN)_6]_{0.9}$) to black ($Li_{0.6}Co^{3+}$ $[Fe^{2+}(CN)_6]_{0.9}$) phases takes place at the phase boundary via selective $Li^+$ deintercalation. We emphasize that the length scale (several tens of μm) of the PS is much longer than that (several hundred nm: see Figs S1 and S2) of the crystal grain size of the film. We consider that the volume contraction due to the phase transformation into the black phase is the main driving force of the macroscopic PS, as schematically shown in Fig. 3(a). In order to confirm this hypothesis, we evaluated the linear expansion coefficient ($\Delta L/L$) between $x = 1.6$ and 1.4. The linear expansions ($\Delta L$) between $x = 1.6$ and 1.4 were evaluated using the spots at the grain boundaries, as shown in Fig. S5. The $\Delta L/L$ value is $-0.013 \pm 0.012$ in the black region [Fig. S4(a)] and $-0.004 \pm 0.013$ in the green region [Fig. S4(b)]. The observed $\Delta L/L$ ($= -0.013$) value in the black phase is quantitatively consistent with that ($= -0.023$) evaluated from the lattice constants of the green and black phase. In other words, the lattice contraction due to the phase transformation propagates beyond the respective grains. Then, the lattice contraction causes a significant strain at the phase boundary. In such a region, the $Li^+$ deintercalation and subsequent phase transformation into the black phase is much easier than nucleation of a new micro-domain of $Li_{0.6}Co^{3+}$ $[Fe^{2+}(CN)_6]_{0.9}$ in another part of the green region. This scenario is essentially the same as the 'domino-cascade model' of $Li_xFePO_4$[14].

The PS dynamics are critically dependent on the film thickness. Figure 4 shows the charge curve of the $Li_xCo[Fe(CN)_6]_{0.9}$ film ($d = 0.5\,\mu m$) at 0.9 C against $x$, together with the microscopic images. In the late stage ($0.6 < x < 0.0$) of the charge curve, a plateau due to the reduction process of $Fe^{2+}$ to $Fe^{3+}$ is observed at around 4.0 V. We observed no trace of the macroscopic PS. The image becomes dark with a decrease in $x$ from $x = 1.6$ to 0.8. This is because parts of $Co^{2+}$ are oxidized to $Co^{3+}$, which is the initial state of the optical transition, with decrease in $x$. With further decrease in $x$ below 0.8, the image becomes bright again. This is because parts of $Fe^{2+}$, which is the final state of the optical transition, are oxidized to $Fe^{3+}$ with decrease in $x$.

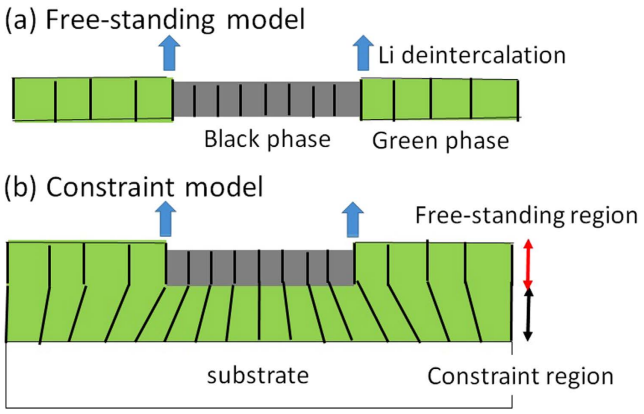


**Figure 3.** Schematic pictures of macroscopic PS in the (**a**) free-standing and (**b**) constraint models. In the constraint model, the bottom parts of the crystal pillars are strongly pinned at the substrate. Green and gray regions represent green and black phases, respectively. Upper arrows and vertical lines represent the selective $Li^+$ deintercalation and crystal grains, respectively.

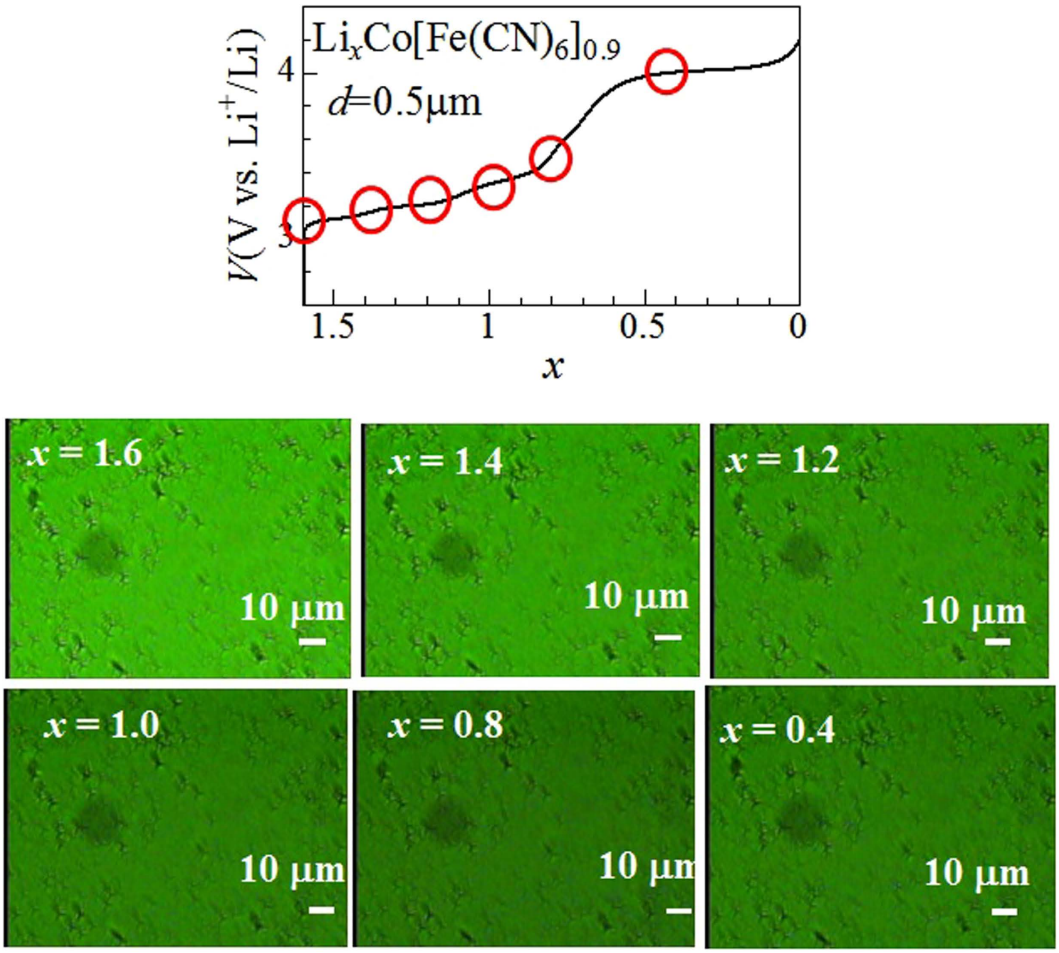


**Figure 4.** Upper panel: charge curve of $Li_xCo[Fe(CN)_6]_{0.9}$ film ($d = 0.5\,\mu m$) at 0.9 C against $x$. Lower panel: microscopic images at the respective $x$, indicated by red circles in the charge curve.

## Normalized Absorption Intensity $I_n$ Against $x$

To investigate the PS dynamics in more detail, we quantitatively investigated the absorption intensity against $x$. Recall that the 540 nm absorption band is ascribed to the electron transfer from $Fe^{2+}$ to the neighboring $Co^{3+}$. Then, the absorption intensity at $x = 1.6$ ($Li_{1.6}Co^{2+}$ $[Fe^{2+}$ $(CN)_6]_{0.9}$) and at $x = 0.6$ ($Li_{0.6}Co^{3+}$ $[Fe^{2+}$ $(CN)_6]_{0.9}$)

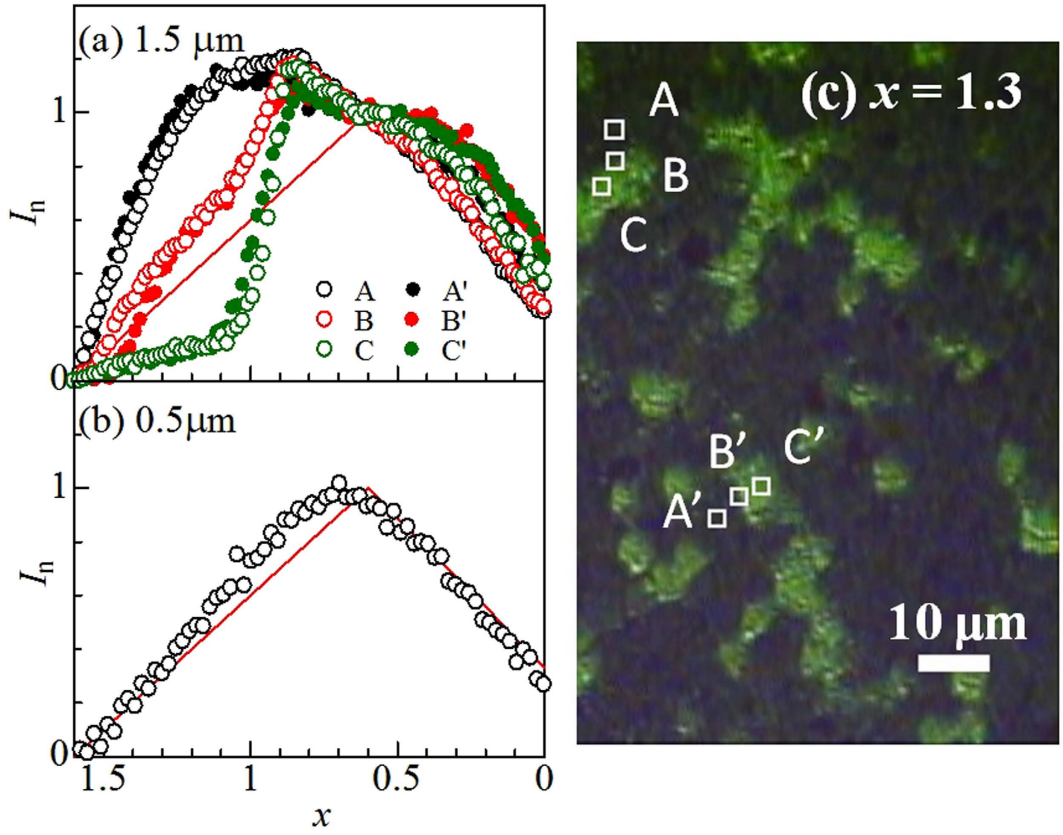


**Figure 5.** (**a**) Normalized absorption intensity ($I_n$) of the $Li_xCo[Fe(CN)_6]_{0.9}$ film against $x$: (**a**) $d = 1.5\,\mu m$ at 0.7 C and (**b**) $d = 0.5\,\mu m$ at 0.9 C. The red lines are results of the mean-field model (see text). (**c**) Microscopic image of the thick film at $x = 1.3$, together with the investigated positions.

should be a minimum and maximum, respectively. Therefore, we defined normalized absorption intensity ($I_n$) as $[I(x) - I(1.6)]/[I(0.6) - I(1.6)]$. Here, we assume a homogeneous Co oxidization in the $x$ range of $1.6 > x > 0.6$ and a homogeneous Fe oxidization in the $x$ range of $0.6 > x > 0.0$ (mean-field model). In this model, $I_n$ is expressed as $1.6 - x$ ($1.6 > x > 0.6$) and $x + 0.4$ ($0.6 > x > 0.0$), because $I_n$ is proportional to the probability of finding the $Co^{3+}$ site adjacent to the $Fe^{2+}$ site. The red lines in Fig. 5(a) and (b) are the results of the mean-field model.

Figure 5(a) shows $I_n$ of the thick film against $x$ in the black (A and A′), phase boundary (B and B′), and green (C and C′) regions. Data were averaged in $2 \times 2\,\mu m^2$ area, as indicated by squares in Fig. 5(c). In the $x$ range of $1.6 > x > 0.6$, the $I_n - x$ curves show significant position dependence and seriously deviate from the mean-field model (red lines). In the $x$ range of $0.6 > x > 0.0$, however, the $I_n - x$ curves overlap each other and nearly obey the mean-field model (red lines). In the black region (A and A′), $I_n$ steeply increases to ~1 with a decrease in $x$ below $x = 1.2$, indicating selective $Li^+$ deintercalation and transformation into the black phase. The increase in $I_n$ gradually saturated below $x = 1.2$, indicating that the black region covers the entire $2 \times 2\,\mu m^2$ square. In the green region (C and C′), $I_n$ remains nearly zero in the $x$ range of $1.6 < x < 1.0$. With further decrease in $x$, $I_n$ steeply increases to ~1, indicating that the phase boundary reaches the square. In the boundary region (B and B′), $I_n$ shows an intermediate behavior between the two limiting cases. The increase of the $I_n - x$ curve, however, is rather gradual. This unexpected behavior implies finite width of the phase boundary due to the gradual change of $x$ and/or inclination of the boundary. Figure 5(b) shows the $I_n - x$ curves of the thin film (0.5 μm) at 0.9 C against $x$: The curve nearly obeys the mean-field model (red lines) in the entire $x$ region, indicating that $Co^{2+}$ and $Fe^{2+}$ are homogeneously oxidized in the respective plateaus in the thin film.

## Discussion

According to classical nucleation theory, Li deficiencies in the parent $Li_{1.6}Co[Fe(CN)_6]_{0.9}$ pool together to form micro-clusters of $Li_{0.6}Co[Fe(CN)_6]_{0.9}$. The cluster deterministically grows when its size stochastically reaches a critical size, which is determined by the balance between the free energy gain due to the transformation and the strain loss at the interface. Unfortunately, the nucleation process is difficult to detect due to the limited spatial resolution ($= 1\,\mu m$) of the optical microscopy. We investigated the microscopic image in the 1st discharge process and found that the black region remains as islands even in the fully discharged state ($Li_{1.6}Co[Fe(CN)_6]_{0.9}$) (the $x = 1.6$ image in Fig. S6). This is in sharp contrast with the initial homogeneous image (the $x = 1.6$ image in Fig. 2) of the ion-exchanged $Li_{1.6}Co[Fe(CN)_6]_{0.9}$. Such islands are probably stabilized by local compression or local Fe deficiency in the film. Thus, physical or chemical inhomogeneity of the cathode materials is advantageous for the PS.

Finally, let us discuss the $d$-dependence of the PS dynamics. If the film were free-standing [Fig. 3(a)] without any constraint, macroscopic PS would be possible even in the thin film. The actual film, however, consists of columnar crystal grains[19]. The bottom parts of the crystal pillars are strongly pinned at the indium tin oxide (ITO) substrate, as schematically shown in Fig. 3(b). We will call this model as "constraint model". Similarly to the case of the 1.5 μm film, we evaluated $\Delta L/L$ between $x = 1.6$ and 1.4. The $\Delta L/L$ value is $-0.002 \pm 0.006$ [Fig. S4(c)]. We observed no detectable displacement in the in-plane direction, which support the constraint model. In the constraint model, the Gibbs free energy change is expressed as $\Delta G = \Delta G_{\text{phase transformation}} + \Delta G_{\text{deformation}}$. The first term is the Gibbs free energy change due phase transformation in the free-standing system, while the second term deformation energy of the pillars. To realize the PS ($\Delta G < 0$), the energy gain ($-\Delta G_{\text{phase transformation}}$) due to the phase transformation and the interfacial strain must surpass the energy loss ($-\Delta G_{\text{deformation}}$) due to the pillar bending. The thicker the film becomes, the smaller $-\Delta G_{\text{deformation}}$ becomes. Thus, the constraint model well explains why the PS appears in the thick film (Fig. 2) but is absent in the thin films (Fig. 4). Judging from the fact the 1.5 μm film shows the PS while the 0.5 μm film does not, the characteristic thickness is order of ~1 μm. Let us evaluate the bending angle at $d = 1$ μm at the phase boundary. The in-plane displacement is 0.1 μm [=10 μm (domain size of the PS) × 0.01($\Delta L/L$ in the black region)]. Then, bending angle becomes 6 degree [=$\sin^{-1}$(0.1 μm/1 μm)]. These arguments imply that the external strain due to the surrounding environment crucially influences the PS dynamics within the respective particle, and hence the cycle and rate properties of the cathode. Here, we point out that the cycle properties is much worse in the $Li_xCo[Fe(CN)_6]_{0.9}$ film[16] as compared with the isostructural $Li_xMn[Fe(CN)_6]_{0.83}$ film[20], which does not shows PS.

**Summary.** We performed *in situ* microscopic observation of PS dynamics in the $Li_xCo[Fe(CN)_6]_{0.9}$ films. The thick film shows a characteristic macroscopic PS of several tens of μm into the original green and secondary black phases below $x < 1.0$. We further found that the PS is absent in the thin film, reflecting the strain due to the substrate. This suggests that the external strain due to the surrounding environment crucially influences the PS dynamics within the respective particles, and hence the cycle and rate properties of the cathode.

## Method

**Fabrication and characterization of $Li_xCo[Fe(CN)_6]_{0.9}$ film.** Thin films of $Li_{1.6}Co[Fe(CN)_6]_{0.9}$ were synthesized by electrochemical deposition of $Na_{1.6}Co[Fe(CN)_6]_{0.9}$ and successive electrochemical ion-exchange. The electrochemical deposition of the $Na_{1.6}Co[Fe(CN)_6]_{0.9}$ film was performed in a three-pole beaker-type cell. The working, counter, and standard electrodes were an indium tin oxide (ITO) transparent, Pt, and standard Ag/AgCl electrodes, respectively. The electrolyte was an aqueous solution containing 0.8 mmol/L $K_3[Fe(CN)_6]$, 0.5 mmol/L $Co(NO_3)_2$, and 5.0 mol/L $Na(NO_3)$. The films were deposited on the ITO electrode under potentiostatic conditions at −0:45 V vs. the Ag/AgCl electrode. The thickness ($d$) of the film was controlled by the deposition time and was determined with a profilometer. The chemical composition of the film was determined by the inductively coupled plasma (ICP) method and CHN organic elementary analysis (PerkinElmer 2400 CHN Elemental Analyzer). The compound contains crystal waters as $Na_{1.6}Co[Fe(CN)_6]_{0.9}2.9\ H_2O$. Na in the film was electrochemically substituted for Li in a two-pole cell under Ar atmosphere in an Ar filled glove box. The anode was Li and the electrolyte was ethylene carbonate (EC)/diethyl carbonate (DEC) solution containing 1 mol/L $LiClO_4$. The charge/discharge rate was about 1 C. The cut-off voltage was from 2.0 to 4.2 V.

The X-ray diffraction patterns of the $Na_{1.6}Co[Fe(CN)_6]_{0.9}$ films were obtained with a Cu Kα lines (Fig. S7). All the reflections can be indexed with the face-centered cubic structure. The lattice constants ($a$) were 1.027 nm for both the films. The morphologies of the $Na_{1.6}Co[Fe(CN)_6]_{0.9}$ films were investigated with atomic force microscopy (AFM: Fig. S1) and scanning electron microscopy (SEM: Fig. S2). The films consist of crystalline grains of several hundred nm in diameter. The cross-sectional SEM image[19] indicates that the respective crystalline grains are columnar.

**Optical battery cell for microscopy.** The optical battery cell has a structure of $Li_{1.6}Co[Fe(CN)_6]_{0.9}$ film on an ITO glass/Teflon sheet with a square hole/anode. The anode was a small piece of Li metal attached on a cupper foil, which was sandwiched between the Teflon sheet and slide glass. The hole in the Teflon sheet was filled with electrolyte. The electrolyte was an ethylene carbonate (EC)/diethyl carbonate (DEC) solution containing 1 mol/L $LiClO_4$. The cell was assembled under Ar atmosphere in an Ar-filled glove box and was sealed with Kapton tape. The charge/discharge behavior of the cell was stable and was consistent with the literature[16] even under air atmosphere for at least ten hours. It is difficult to precisely evaluate the capacity due to the bubbles of Ar gas which were inevitably introduced in the hole. Actually, some parts of the $Li_{1.6}Co[Fe(CN)_6]_{0.9}$ film remained unchanged during the charge/discharge process. Therefore, we assume a fully charged and fully discharged state of $x = 0.0$ and 1.6, respectively.

***In situ* microscopic observation of the PS dynamics.** The *in situ* microscopic PS dynamics were recorded with a microscopy system equipped with a charge-coupled device (CCD) camera for moving images. A halogen lamp was monochromized with a dichroic filter (DIF-50S-GRE: Sigma Koki, Co Ltd.) and used as the probe light source. The transmission range of the filter was 515–560 nm. The spatial resolution of the system was 1 μm. The probe light sensitively monitored the absorption band due to the electron transfer from $Fe^{2+}$ to neighboring $Co^{3+}$. The absorbance intensity $I(x)$ at $x$ is expressed as $-1/d \times \ln[T(x)/T_0]$, where $d$, $T(x)$, and $T_0$, are the film thickness, transmitted light intensity at $x$ and incident light intensity. $T(x)$ was evaluated by the chromaticity of the green color. The normalized absorbance intensity ($I_n$), $[I(x) - I(1.6)]/[I(0.6) - I(1.6)]$, is expressed as $[\ln T(x) - \ln T(1.6)]/[\ln T(0.6) - \ln T(1.6)]$. To increase the signal-to-noise ratio, the chromaticity was averaged within 8 × 8 pixels (2 × 2 μm$^2$ area) around each position.

## References


1. Tarascon, J. M. & Armand, M. Issues and challenges facing rechargeable lithium batteries. *Nature* **414,** 359–367 (2001).
2. Armand, M. & Tarascon, J. M. Building better batteries. *Nature* **451,** 652–657 (2008).
3. Reimers, J. N. & Dahn, J. R. Electrochemical and *in situ* X-ray-diffraction studies of lithium intercalation in $Li_xCoO_2$. *J. Electrochem. Soc.* **139,** 2091–2097 (1992).
4. Thackeray, M. M., Johnson, P. J., Depicciotto, L. A., Bruce, P. G. & Goodenough, J. B. Electrochemical extraction of lithium from $LiMn_2O_4$. *Mater. Res. Bull.* **19,** 179–187 (1984).
5. Ohzuku, T. & Makimura, Y. Layered lithium insertion material of $LiCo_{1/3}Ni_{1/3}Mn_{1/3}O_2$ for lithium-ion batteries. *Chem. Lett.* **30,** 642–643 (2001).
6. Padhi, A. K. Nanjundaswamy, K. S. & Goodenough, J. B. Phospho-olivines as positive-electrode for rechargeable lithium battries. *J. Electrochem. Soc.* **144,** 1188–1194 (1997).
7. Delacourt, C., Poizot, P., Tarascon, J. M. & Masquelier, C. The existence of a temperature-driven solid solution in $Li_xFePO_4$ for $0 < x < 1$. *Nature Mater* **4,** 254–260 (2005).
8. Dodd, J. L., Yazami, R. & Fultz, B. Phase diagram of $Li_{(x)}FePO_4$. *Electrochem. Solid State Lett.* **9,** A151–155 (2006).
9. Zhou, F., Maxisch, T. & Ceder, G. Configurational electronic entropy and the phase diagram of mixed-valence oxides: The case of $Li_xFePO_4$. *Phys. Rev. Lett.* **97,** 155704 (2006).
10. Yamada, A. *et al.* Room-temperature miscibility gap in $Li_xFePO_4$. *Nature Mater.* **5,** 357–360 (2006).
11. Kang, B. & Ceder, G. Battery materials for ultrafast charging and discharging. *Nature* **458(7235),** 190–193 (2009).
12. Chen, G. Y., Song, X. Y. & Richardson, T. J. Electron microscopy study of the $LiFePO_4$ to $FePO_4$ phase transition. *Electrochem. Solid State Lett.* **9,** A295–298 (2006).
13. Cogswell, D. A. & Barant M. Z, Coherency strain and the kinetics of phase separation in $LiFePO_4$ nanoparticles. *ACS Nano* **3,** 2215–2225 (2012).
14. Delmas, C., Maccario, M., Croguennec, L., Le Cras, F. & Weill, F. Lithium deintercalation in $LiFePO_4$ nanoparticles via a domino-cascade model. *Nature Mater.* **7,** 665–671 (2008).
15. Malik, R., Zhou, F. & Ceder G. Kinetics of non-equilibrium lithium incorporation in $LiFePO_4$. *Nature Mater.* **10,** 587–590 (2011).
16. Takachi, M. & Moritomo, Y. Structural, electronic and electrochemical properties of $Li_xCo[Fe(CN)_6]_{0.90}$ $2.9H_2O$. *Jpn. J. Appl. Phys.* **52,** 144301 (2013).
17. Kurihara, Y. *et al.* Electronic structure of hole-doped transition metal cyanides. *J. Phys. Soc. Jpn.* **79,** 144710 (2010).
18. Izumi, F. & Momma, K. Three-dimensional visualization in powder diffraction. *J. Solid State Phemom.* **130,** 15–20 (2007).
19. Shibata, T. & Moritomo, Y. Electronic properties of all solid ion-transfer device fabricated with transition metal cyanide films. *Jpn. J. Appl. Phys.* **49,** 094101 (2010).
20. Matsuda, T. & Moritomo, Y. Thin film electrode of Prussian blue analogue for Li-ion battery. *Appl. Phys. Express.* **4,** 147101 (2011).


## Acknowledgements

This work was supported by the Yazaki Memorial Foundation for Science and Technology and Nippon Sheet Glass Foundation for Materials Science and Engineering. The elementary analyses were performed at the Chemical Analysis Division, Research Facility Center for Science and Engineering, University of Tsukuba. We are grateful to Dr. Shibata for his help in the SEM measurements. The synchrotron-radiation X-ray powder diffraction experiments were performed at the SPring-8 BL02B2 beamline with the approval of the Japan Synchrotron Radiation Research Institute (JASRI).

## Author Contributions

Y.M. planned the investigation overall and wrote the manuscript. M.T. performed all the experiments and analyses, including the fabrication and characterization of the thin films.

## Additional Information

**Supplementary information** accompanies this paper at http://www.nature.com/srep

**Competing financial interests:** The authors declare no competing financial interests.

**How to cite this article**: Takachi, M. and Moritomo, Y. *In situ* observation of macroscopic phase separation in cobalt hexacyanoferrate film. *Sci. Rep.* **7**, 42694; doi: 10.1038/srep42694 (2017).

**Publisher's note:** Springer Nature remains neutral with regard to jurisdictional claims in published maps and institutional affiliations.